Received 23 July 2025; revised 30 August 2025; accepted 1 September 2025. Date of publication 8 September 2025; date of current version 24 November 2025.

Digital Object Identifier 10.1109/OJAP.2025.3606889

Design and Experimental Validation of a Through-Quartz Via-Based LC RIS for Dual-Polarization Beam Steering in Sub-Terahertz Bands

BYEONGJU MOON [1,2] (Student Member, IEEE), SEUNGWOO BANG [1,2] (Graduate Student Member, IEEE), SEONGWOOG OH [3] (Member, IEEE), AND JUNGSUEK OH [1,2] (Senior Member, IEEE)

[1]Institute of New Media and Communications, Seoul National University, Seoul 08826, South Korea
[2]Department of Electrical and Computer Engineering, Seoul National University, Seoul 08826, South Korea
[3]School of Electrical and Computer Engineering, University of Seoul, Seoul 02504, South Korea

CORRESPONDING AUTHOR: J. OH (e-mail: jungsuek@snu.ac.kr)

This work was supported in part by the Samsung Research Funding Center of Samsung Electronics (50%) under Project SRFC-TE2103 and in part by the Institute of Information and Communications Technology Planning and Evaluation (IITP) grant funded by the Korean Government (MSIT) through the Innovative Fusion Technologies of Intelligent Antenna Material/Structure/Network for THz 6G, (50%) under Grant 2021-0-00763.
(Seongwoog Oh and Jungsuek Oh contributed equally to this work.)

ABSTRACT This paper presents a liquid crystal (LC)-based reconfigurable intelligent surface (RIS) capable of simultaneously achieving dual-polarization conversion and beam steering, enabled by through-quartz vias (TQVs). The proposed RIS offers two primary functionalities-dynamic beam steering and polarization conversion-both of which are validated through full-wave simulations and experimental measurements. A tunable LC layer is employed as the dielectric substrate for each unit cell to facilitate beam steering, while bias lines are used to apply external electric fields to the LC medium. To prevent degradation in polarization conversion performance, the bias lines are connected to the patterned copper structures via TQVs embedded within the quartz substrate. The quartz substrate is perforated using a precision sanding technique to form the vias. A 50×50-element LC-based RIS is fabricated using a standard display manufacturing process to ensure uniform LC layer thickness across the array. The results demonstrate that the polarization of an incident wave is converted to its orthogonal counterpart upon reflection from the proposed RIS. Furthermore, by implementing a phase gradient spanning 137° across the unit cells, anomalous reflection is achieved. Comparative measurements with and without the RIS confirm that the received power is significantly enhanced in the direction corresponding to the RIS-engineered reflection angle.

INDEX TERMS Beam steering, liquid crystals (LCs), metasurface design, polarization conversion, reconfigurable intelligent surface (RIS), sub-terahertz (Sub-THz) communications, through-quartz vias (TQVs), 6G wireless systems.

I. INTRODUCTION

THE advancement of sixth-generation (6G) wireless systems is primarily driven by the objective of delivering ubiquitous, high-speed wireless connectivity without compromise. Currently, the upper mid-band (7–24 GHz) and the sub-terahertz (sub-THz) spectrum (92–300 GHz) have garnered significant attention as key enablers for 6G communication [1]. In particular, the sub-THz band is envisioned as a pivotal solution to mitigate the ongoing challenges of spectrum scarcity and capacity limitations in contemporary wireless networks [2], [3], [4]. This frequency domain offers the potential to support ultra-high data rates, ranging from several tens of gigabits per second to beyond one terabit per second. Despite its promise, the sub-THz band is hindered by a fundamental limitation-its restricted communication range-primarily

caused by severe free-space path loss inherent to these high frequencies [5].

To address the aforementioned limitations, the concept of reconfigurable intelligent surfaces (RISs) has emerged as a key enabler and extensively explored topic in the context of 6G wireless communication systems. RIS technology, characterized by its adaptability and versatility, is engineered to function effectively in both indoor and outdoor environments. Its primary function is to dynamically manipulate electromagnetic waves by leveraging its reflective properties, thereby circumventing physical obstructions and enhancing signal coverage in shadowed or previously inaccessible regions. This capability not only improves link reliability but also optimizes the utilization of spectral and spatial resources, positioning RISs as a transformative solution in the 6G paradigm. RISs can support multiple operational modes, including reflection, refraction, absorption, polarization manipulation, and data modulation, thereby enabling high-quality wireless transmission [6]. Among these functionalities, polarization conversion is particularly desirable for sub-terahertz (sub-THz) and higher frequency bands, as it facilitates a wide range of applications such as terahertz imaging and nondestructive material inspection [7], communication multiplexing [8], biomedical detection [9], radar sensing [10], and security systems [11].

A typical RIS architecture consists of an array of unit cell elements, often numbering in the hundreds, arranged in a periodic configuration. Each unit cell generally comprises a microstrip patch printed on a dielectric substrate with a thickness less than one-tenth of the operating wavelength ($\lambda/10$) [12]. These RISs are typically deployed in proximity to a ground plane. To suppress grating lobes and ensure effective beam manipulation, the unit cells are spaced at intervals smaller than half of the operating wavelength ($\lambda/2$). To engineer a desired reflected field pattern, it is essential to compute the appropriate phase distribution across the RIS aperture and assign the corresponding phase value to each unit cell. This is typically achieved by tuning the resonant frequency of each patch element. Various reconfiguration mechanisms have been proposed for phase control, including positive-intrinsic-negative (PIN) diodes, varactor diodes, power amplifiers (PAs), and integrated phase shifters [13], [14], [15]. In [13], a light-controlled reflectarray incorporating both PIN diodes and photodiodes was demonstrated. The photodiodes generated control signals upon exposure to light, which were then used to modulate the ON/OFF states of the PIN diodes. This work successfully validated the feasibility of large-scale RIS implementations based on PIN diode technology. In [14], a varactor-diode-based RIS was introduced. Unlike PIN diodes, varactor diodes enable continuous phase tuning, thereby mitigating quantization-induced losses. A unit cell with strong angular stability-achieved via a vertical interconnect access (VIA) wall-was proposed, and a phase gradient was realized using varactor-based control. The angular reciprocity of the RIS was confirmed experimentally, demonstrating reliable performance under oblique incidence up to 60°. Additionally, an active RIS employing a power amplifier (PA) was presented in [15]. In this design, the PA was integrated with a power divider to amplify the reflected signal, thereby improving the link budget by enhancing the signal amplitude.

Despite recent advancements, it is important to note that the RIS implementations reported in the aforementioned studies primarily operate at frequencies below 100 GHz. The application of diodes and amplifiers at sub-terahertz (sub-THz) frequencies is significantly limited due to inherent drawbacks, including high insertion loss, narrow operational bandwidth, nonlinearity, and frequency dispersion [16], [17], [18]. Moreover, realizing multi-bit phase quantization with PIN diodes requires a large number of switching elements, while varactor-diode-based unit cells demand complex biasing circuitry [16], [17], [18]. Additionally, diode-based RISs face scalability challenges arising from high manufacturing costs, packaging complexity, and elevated power consumption. A particularly critical limitation is the lack of commercially available diodes that operate efficiently in the sub-THz regime [19].

As a promising alternative, liquid crystals (LCs) have been adopted as the reconfigurable medium in this work. LCs offer several advantages over conventional tuning components: (1) cost efficiency, attributed to the inverse relationship between frequency and antenna aperture size-higher frequencies result in smaller apertures, thereby reducing the required volume of LC material and enabling compact biasing circuitry compatible with mature liquid crystal display (LCD) fabrication processes; (2) low thermal dissipation, owing to voltage-controlled operation and minimal power consumption in the control electronics; and (3) continuous and wide-range phase tunability with minimal insertion loss, ensuring high reconfigurability and low signal degradation [20].

This paper proposes a RIS designed for polarization conversion using LC technology. The proposed metasurface structure enables simultaneous dual-polarization conversion, whereby transverse electric (TE) polarization is converted to transverse magnetic (TM) polarization and vice versa. Simulation results indicated that similar to previous LC-based metasurfaces utilizing quartz substrates, placing the bias lines on the same side as the metallic electrodes substantially deteriorates the polarization conversion performance due to unintended electromagnetic coupling and altered field distribution. To address this limitation, a through-quartz via (TQV) structure is introduced to route the bias lines through the substrate, thereby preserving the polarization conversion capability.

The unit cells are engineered to collectively realize a surface capable of adaptive beamforming and dual-polarization conversion. The results of this work highlight a promising pathway for the deployment of RIS technology in sub-THz 6G communication systems, particularly for multi-directional integration scenarios, as illustrated in Fig. 1.

The remainder of this paper is organized as follows. Section II presents the design and full-wave simulation

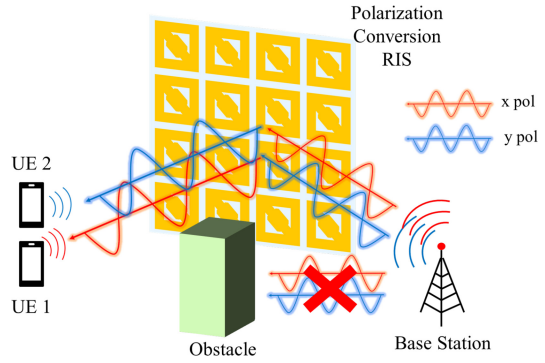

FIGURE 1. Conceptual diagram of the proposed LC-based RIS operating in sub-THz frequency bands for 6G wireless communication systems.

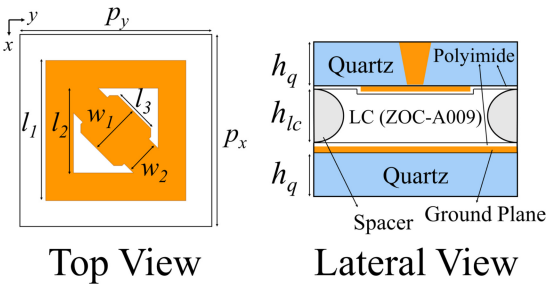

FIGURE 2. Top and lateral views of the proposed LC-based RIS unit cell for polarization conversion.

TABLE 1. Design parameters of proposed unit cell and their values.

Parameters	Values [mm]	Parameters	Values [mm]
p_x	0.8	w_1	0.2
p_y	0.8	w_2	0.12
l_1	0.48	h_q	0.5
l_2	0.29	h_{lc}	0.045
l_3	0.16		

results of the LC-based polarization-conversion unit cell. The fabrication procedure of the proposed RIS is detailed in Section III. Section IV provides the measured responses of the unit cell and experimental validation of the RIS. Finally, conclusions are drawn in Section V.

II. DESIGN AND ANALYSIS OF LC-BASED RIS UNIT CELL

A. POLARIZATION-CONVERSION UNIT CELL WITH LIQUID CRYSTALS

The proposed dual-polarization conversion unit cell utilizing LCs is depicted in Fig. 2. The structure consists of a quartz wafer, a patterned metal layer for polarization conversion, a metallic ground plane, and an LC layer sandwiched between them. A thin polyimide alignment layer is coated on the ground plane, while the metal pattern aligns the LC molecules along the x-axis. To achieve uniform LC orientation, the rubbing directions are set to $-x$ on the patterned metal side and $+x$ on the ground plane side.

The LC material employed is ZOC-A009XX, a custom LC mixture developed by JNC for RF applications. According to the manufacturer's datasheet, its dielectric constant and loss tangent are 2.5 and 0.014, respectively, under zero bias, and 3.44 and 0.004 when fully biased at 28 GHz for both perpendicular and parallel polarizations. Although this study targets the sub-THz regime, relevant dielectric property data for ZOC-A013XX-another LC mixture from the same manufacturer-were reported in [21]. Based on these findings, the relative permittivity is varied from 2.5 (zero bias) to 3.5 (fully biased), with a corresponding loss tangent of $\tan\delta = 0.023$ for both states. The substrate used is VIOSIL-SQ, a high-purity quartz material manufactured by Shin-Etsu, which exhibits a complex permittivity of 3.9 and a loss tangent of 0.0007 at 60 GHz. The detailed structural parameters of the proposed unit cell are summarized in Table 1. The unit cell size is set to 0.37λ to suppress grating lobes and ensure robust performance under oblique incidence.

The metallic pattern printed on the quartz substrate serves as the polarization-conversion structure. The polarization conversion mechanism of the proposed unit cell is illustrated in Fig. 3. An x-polarized plane wave incident along the z-axis can be expressed as [22]

$$\vec{E}_i = \hat{x}E_{ix}e^{-jkz} \tag{1}$$

where E_{ix} and k represent the amplitude and the propagation constant, respectively. As shown in Fig. 3, the xy coordinate system can be transformed into a rotated uv coordinate system, and the basis vectors are related as follows:

$$\hat{x} = \hat{u}\cos\theta - \hat{v}\sin\theta \tag{2}$$

$$\hat{y} = \hat{u}\sin\theta + \hat{v}\cos\theta \tag{3}$$

Using this transformation, the reflected electric field $\vec{E}_r$ can be expressed as:

$$\vec{E}_r = \left[\hat{x}\cos 2\theta + \hat{y}\sin 2\theta\right]E_{rx}e^{j\phi_x}e^{jkz} \tag{4}$$

when the phase difference satisfies $|\phi_x - \phi_y| = 180°$.

From (4), a reference angle of $\theta = 45°$ introduces the necessary asymmetry to enable polarization conversion between the x-polarized incident wave and the y-polarized reflected wave, and vice versa. To satisfy this condition, the proposed unit cell incorporates a ring-shaped patch with a diagonally oriented stub at 45°. The ring structure gives rise to dual resonance points, contributing to a broadband frequency response. The diagonal stub facilitates polarization conversion, while an additional octagonal patch is embedded at the center of the stub. The function of this octagonal patch will be further discussed in the following section.

Full-wave electromagnetic simulations based on the Floquet mode analysis were carried out using ANSYS HFSS to evaluate the polarization-conversion characteristics at the unit cell level. Fig. 4 shows the simulated frequency response of the unit cell under different LC biasing conditions. The polarization conversion performance is specifically illustrated in Fig. 4(a). The magnitude of the x-to-y polarization component is observed to be higher than

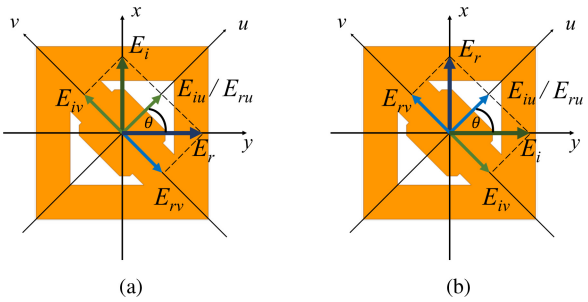

FIGURE 3. Conceptual illustration of polarization conversion using the proposed metallic pattern: (a) *x*-to-*y* polarization conversion and (b) *y*-to-*x* polarization conversion.

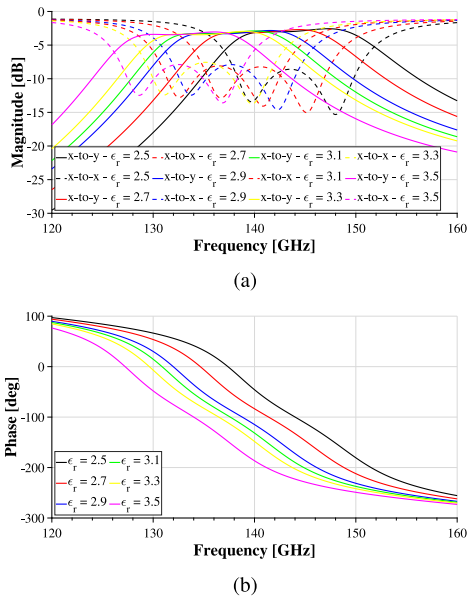

FIGURE 4. Simulated frequency responses of the proposed unit cell for varying LC permittivity values (from 2.5 to 3.5 in 0.2 increments). (a) Reflection magnitude for *x*-to-*y* and *x*-to-*x* polarizations; (b) phase response for *x*-to-*y* polarization.

that of the *x*-to-*x* component, indicating effective polarization conversion achieved by the proposed structure. Due to the dual-ring geometry, two distinct resonance points appear in the *x*-to-*x* polarization reflection. Under the fully biased state, these resonances are located at 128.6 GHz and 136.9 GHz, with corresponding reflection magnitudes of −12.48 dB and −13.59 dB, respectively. This dual-resonance behavior results in a wideband polarization conversion response for the *x*-to-*y* component. At 138 GHz, the proposed unit cell exhibits a phase tuning range of 146.4°, which is sufficient for beam steering applications. It is also worth noting that the *y*-to-*x* and *y*-to-*y* polarization responses display similar characteristics; however, these results are omitted for brevity.

B. UNIT CELL WITH BIAS LINE UTILIZING THROUGH-QUARTZ VIA (TQV)

The effective permittivity of LC varies as the LC molecules reorient in response to the magnitude and direction of an externally applied electric field [23]. In other words, modulation of the LC permittivity requires the application

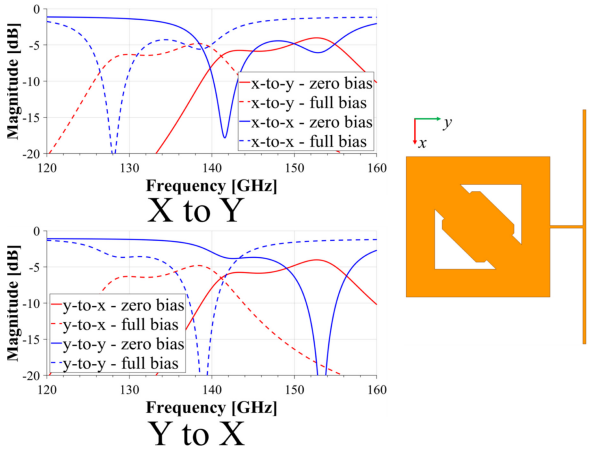

FIGURE 5. Simulated reflection magnitude of the proposed unit cell with a bias line directly connected to the polarization-conversion structure.

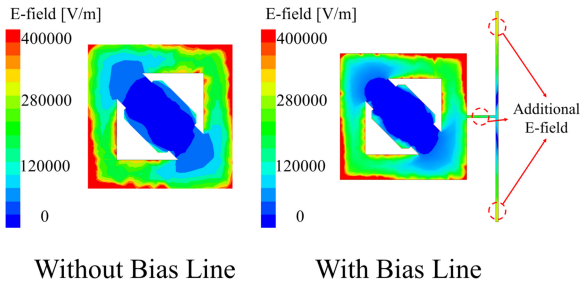

FIGURE 6. Simulated electric field distribution of the unit cell with and without a directly connected bias line.

of a DC bias voltage across the LC layer. To enable this, a bias line must be introduced to deliver the DC voltage to the metal patch situated above the LC.

The most straightforward method, as proposed in [24], is to directly connect the bias line to the metal pattern. However, in the case of the proposed unit cell, this approach resulted in a notable degradation in polarization-conversion performance. Fig. 5 shows the simulated frequency response for the unit cell with a directly connected bias line. In this configuration, the bias line is aligned along the *x*-axis with a width of 0.01 mm.

For the *x*-to-*y* and *x*-to-*x* polarization responses under fully biased conditions, the resonance frequencies are observed at 127.9 GHz and 138.7 GHz, with reflection magnitudes of −19.85 dB and −5.58 dB, respectively. For the *y*-to-*x* and *y*-to-*y* responses, the corresponding resonance points occur at 129 GHz and 139 GHz, with magnitudes of −3.67 dB and −24.8 dB, respectively. Fig. 6 illustrates the electric field distribution of both the original unit cell and the modified version with a directly connected bias line. In the baseline design, the electric field is concentrated at the four corners of the ring patch and strongly localized within the inner ring on the side opposite to the stubs. These field concentrations are responsible for generating the dual resonance behavior discussed previously.

In contrast, the modified unit cell exhibits additional field concentrations at the junction between the metal patch

and the bias line, as well as at both ends of the bias line. These unintended fields interfere with the natural field distribution of the ring structure, thereby weakening the outer ring resonance, particularly affecting the low-frequency resonance in the y-to-x response. Furthermore, the end effects introduced by the bias line degrade both resonance points in the x-to-y polarization conversion. These results confirm that directly connecting the bias line to the metal patch significantly deteriorates the polarization-conversion characteristics.

To mitigate the performance degradation caused by direct bias-line connections, a TQV technique was adopted for bias voltage delivery [23]. The unit cell incorporating a TQV-based bias line is illustrated in Fig. 7. The TQV is strategically placed at the center of the metallic pattern, where the electric field intensity is relatively weak. An octagonal-shaped patch is introduced as the via pad to accommodate the TQV. The use of a rectangular or square pad was found to be suboptimal, as its corners overlap with the inner ring structure, inducing parasitic current paths that adversely affect the frequency response. The corner-truncated (octagonal) design mitigates this issue by reducing unwanted coupling.

The upper portion of the TQV is connected to the bias pad through a narrow bias line. The geometric parameters of the TQV and associated biasing elements are as follows: $r_t = 0.3$ mm, $r_l = 0.1$ mm, $l_{\text{pad}} = 0.35$ mm, $l_{\text{bias}} = 0.175$ mm, and $w_{\text{bias}} = 0.01$ mm.

Fig. 8 presents the simulated electric field distribution around the polarization-conversion structure and the bias pad with the TQV bias line. Compared with the configuration shown in Fig. 6, the revised design does not exhibit any observable additional electric field concentrations near the bias line or pad, resulting in performance closely matching that of the unit cell without any bias line. The simulated frequency response of the TQV-integrated unit cell is shown in Fig. 9. The resonance frequency is slightly shifted upward due to the minor influence of the TQV on the inner ring's electric field distribution. Moreover, the magnitude response also changes, primarily as a result of the modified field distribution between the inner and outer rings. A more detailed field analysis indicates that the electric field on the stub-free side of both rings is significantly intensified.

Consequently, the x-to-y polarization conversion bandwidth-defined using a -6 dB reference-extends from 138.1 GHz to 141.69 GHz, resulting in a bandwidth of 3.59 GHz. This bandwidth is marginally wider than that of the structure without the TQV. Although the phase tuning range slightly decreases to 160° due to the presence of the TQV and bias pad, it remains sufficient to enable beam steering functionality.

C. OBLIQUE INCIDENCE RESPONSE

For RIS-assisted wireless communication, angular stability is a critical design factor, as incident waves may arrive from various directions. Therefore, it is essential to evaluate the magnitude and phase response of the proposed unit cell under oblique incidence. Based on the coordinate system defined in Fig. 7, the incidence angle θ is varied from 0° to 60°.

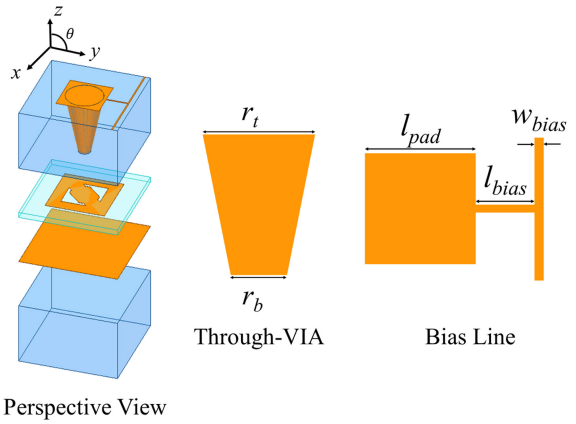

FIGURE 7. Structural configuration of the proposed unit cell with a TQV bias line.

Fig. 10 shows the simulated reflection magnitude and phase responses of the unit cell for different LC biasing states under oblique incidence. For the x-to-y polarization component, at normal incidence ($\theta = 0°$), one of the operating points under full bias is located at 138.2 GHz with a reflection magnitude of -1.55 dB. At an oblique angle of 60°, the corresponding resonance shifts to 138.9 GHz, with a magnitude of -3.15 dB. Around 140 GHz, the magnitude variation remains moderate, ranging from -3.52 dB at 0° to -5.07 dB at 60°. While more noticeable variations appear at other resonance points, they are not critical to system operation and thus can be disregarded. With respect to a -1 dB reference for stable operation, the magnitude response of the x-to-y polarization remains relatively consistent up to 45°: -3.58 dB at 0°, -3.83 dB at 20°, -4.08 dB at 30°, -4.28 dB at 40°, and -4.45 dB at 45°. The corresponding phase response at 140 GHz also remains within acceptable limits. Under full bias, the phase varies from $-30.82°$ at 0° to $-9.26°$ at 60°. In the zero bias condition, the phase shifts from $-193.73°$ to $-185.92°$ over the same angular range. For the y-to-x polarization response, the behavior at frequencies above 150 GHz deviates slightly when θ exceeds 45°; however, it remains consistent with the trend observed in the x-to-y case. Notably, the phase response at 140 GHz is identical for both x-to-y and y-to-x conversions.

In conclusion, the proposed unit cell demonstrates angular stability up to 45° incidence for both x-to-y and y-to-x polarization conversions, making it suitable for practical RIS deployments under diverse propagation conditions.

III. RIS FABRICATION

To experimentally validate the numerical predictions, an LC-based RIS composed of 50 × 50 identical dual-polarization conversion unit cells was fabricated. Each substrates panel measures 55 mm × 50 mm. After L-shaped assembly, the overall RIS dimension becomes 55 mm × 55 mm, where the additional 5 mm is reserved for exposing the connection

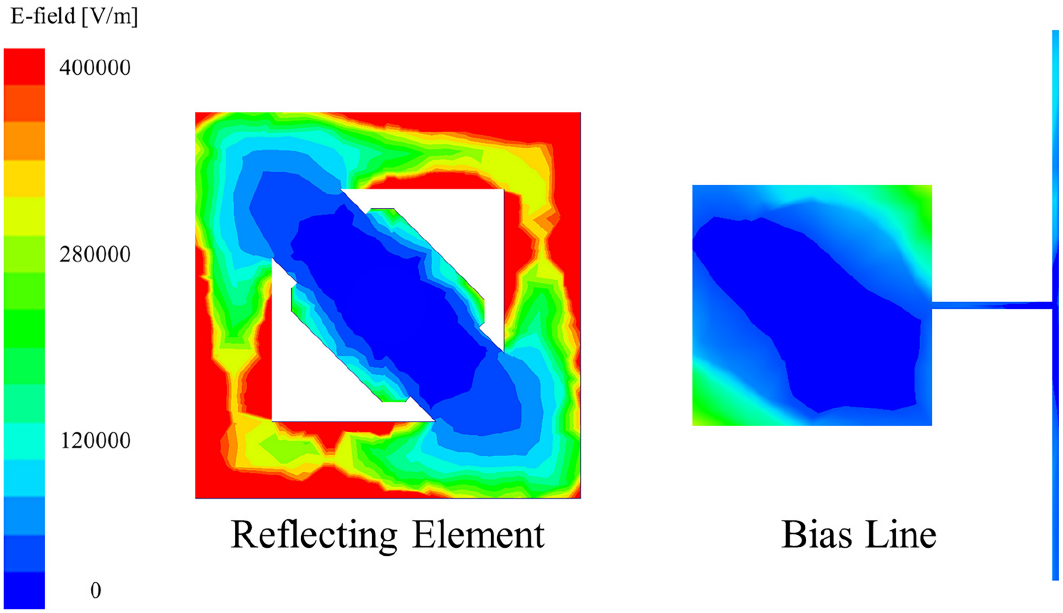

FIGURE 8. Simulated electric field distribution of the unit cell and bias pad with a TQV-based bias line at 138 GHz.

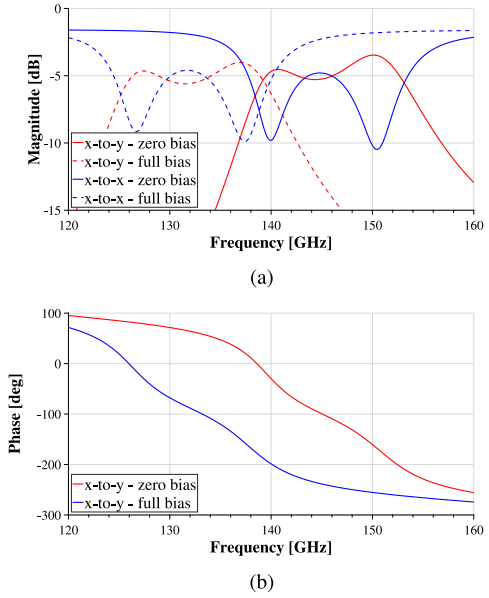

FIGURE 9. Simulated frequency responses of the proposed unit cell with a TQV-based bias line for varying LC bias states: (a) reflection magnitude for *x*-to-*y* and *x*-to-*x* polarizations; (b) phase response for *x*-to-*y* polarization.

pads. Fig. 11 illustrates the multilayer structure of the fabricated RIS. Fig. 11(a) shows the bottom quartz substrate, which is coated with a continuous metal layer acting as the ground plane. Fig. 11(b) presents the top quartz substrate, with the lower surface patterned with the polarization-conversion structure and the upper surface equipped with bias pads and bias lines. A magnified view confirms that the metal patterns for the bias pads and polarization converters were etched according to the design specifications. Minor scratches on the quartz substrate are observed due to mechanical impacts during the fabrication process. TQVs were employed to establish electrical connections between the metal patches and the bias pads, enabling efficient voltage control of the LC medium. As shown in Fig. 11(b), the unit cells are connected in a column-wise configuration. Consequently, the fabricated RIS operates as a one-dimensional (1D) beam scanning reflector, suitable for angular steering in a single plane.

The fabrication of LC-based antennas involves a series of intricate processes, and the manufacturing of the proposed LC RIS is no exception. The entire procedure is divided into three main stages: (1) TQV formation, (2) metal deposition, and (3) LC injection. Each step is described in detail in the following subsections.

TQVs have been proposed as a promising alternative to through-silicon vias (TSVs), owing to their ultrahigh resistivity, low dielectric constant, minimal loss tangent, and compatibility with cost-effective panel-level manufacturing processes [25], [26], [27], [28]. These characteristics become increasingly advantageous as communication frequencies advance into higher bands, where TQVs exhibit superior electrical performance.

With the growing adoption of TQV technology, various formation techniques have been developed, including laser-based drilling [29], and methods utilizing metal wires and magnetic fields [30]. However, most of these techniques are optimized for quartz substrates with thicknesses up to 300 μm, and extending their application beyond this limit presents significant challenges.

To accommodate a stable LC injection process, the proposed structure utilizes a 500 μm-thick quartz substrate, necessitating the use of a mechanical sanding technique for via formation. In this approach, sphere-shaped silicon carbide (SiC) particles with a diameter of 30 μm are employed as

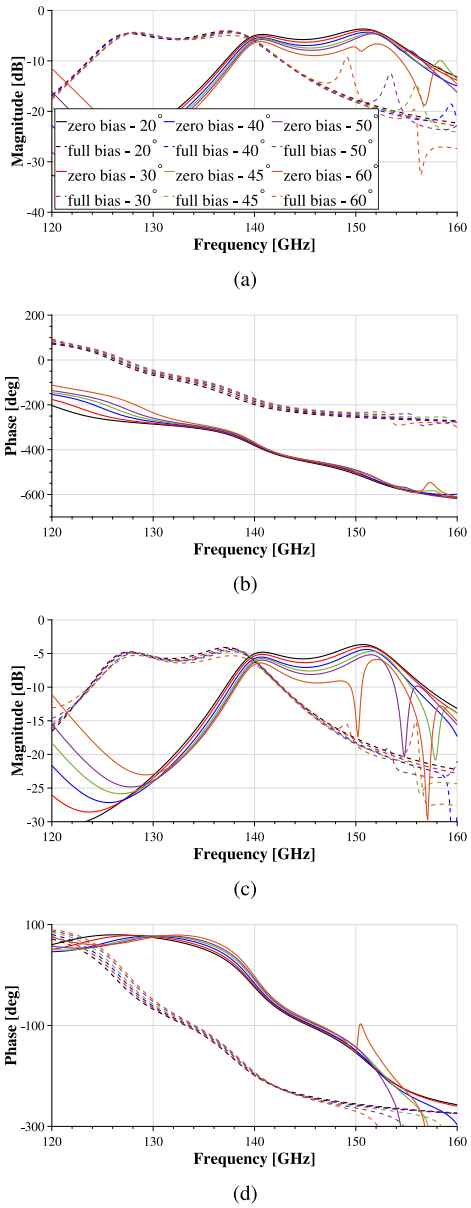

FIGURE 10. Simulated frequency responses of the unit cell under varying incident angles: (a) magnitude response for *x*-to-*y* polarization; (b) phase response for *x*-to-*y* polarization; (c) magnitude response for *y*-to-*x* polarization; (d) phase response for *y*-to-*x* polarization.

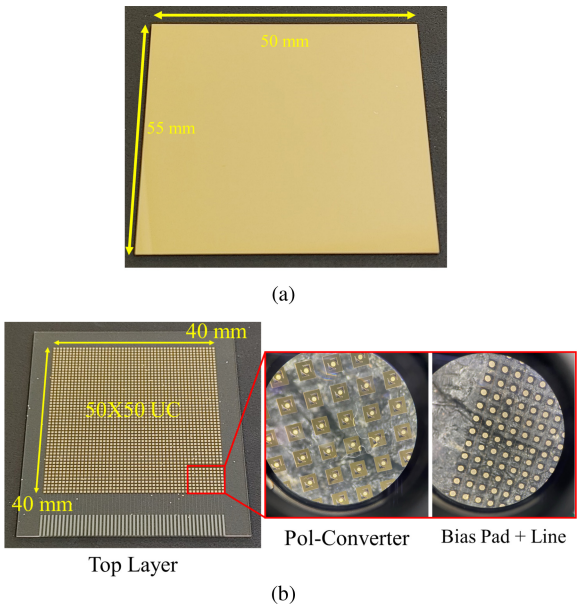

FIGURE 11. Photograph of the fabricated 50 × 50 LC-based RIS sample. (a) Bottom quartz substrate with metal ground plane; (b) top substrate containing the polarization-conversion pattern, TQV, and bias lines, including a magnified view.

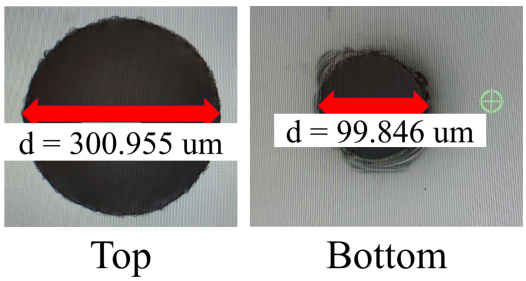

FIGURE 12. Microscopic image of the fabricated TQV structure, exhibiting a tapered profile with an approximate 3:1 diameter ratio between the top and bottom openings.

abrasive media to drill holes into the substrate. A 50 µm-thick dry film, pre-patterned with registration holes, is laminated onto a 4-inch quartz wafer to define the TQV locations. SiC particles are positioned within these holes, and the wafer is subjected to high pressure, driving the particles through the quartz substrate. As the mechanical force diminishes during drilling, the resulting via assumes a truncated conical profile, with a larger diameter at the entry point and a smaller diameter at the exit. Fig. 12 shows a microscopic image of the fabricated TQV, captured using an Olympus MX61A inspection system. Dimensional analysis using the built-in software indicates an upper diameter of 300.955 µm and a lower diameter of 99.846 µm, closely matching the design values of 300 µm and 100 µm used in electromagnetic simulations. Following via formation, a copper seed layer is sputtered onto the inner sidewalls to facilitate charge conduction during electroplating. This seed layer plays a critical role in enabling uniform copper growth throughout the via. Electrolytic copper plating is then performed to complete the TQV formation. For process convenience, the TQV depth is intentionally extended slightly beyond the nominal 500 µm substrate thickness.

After the TQV formation, a chemical mechanical planarization (CMP) process was performed to remove surface irregularities and flatten the via bumps. Subsequently, metallic layers-including polarization-conversion structures and bias pads-were deposited on top of the TQV.

Direct bonding between dissimilar materials can lead to substantial interfacial resistance due to mismatches in chemical and electrical properties. To mitigate this issue, a gradual transition from a non-metallic to a metallic state is required at the interface. This is typically achieved through the introduction of a barrier metal layer, which plays a critical

role in stabilizing the contact characteristics. The metal deposition was carried out using a photolithographic patterning process. A 20-nm-thick titanium layer was deposited via plasma-enhanced chemical vapor deposition (PECVD) to serve as the barrier metal. A subsequent 500-nm-thick copper layer was sputtered on top of the titanium layer to form the primary conductor. To prevent surface oxidation and ensure long-term conductivity, a 20-nm-thick gold layer was electroplated over the copper surface. Upon completion of the metal deposition, the quartz wafers were diced into individual RIS panels measuring 55 mm × 50 mm using a precision diamond cutter.

The final step in the fabrication process is LC injection. Prior to injection, the electrical continuity between the metal pattern and the bias pad was verified using a multimeter to ensure successful TQV formation. Out of 2,500 unit cells, 52 exhibited open circuits, corresponding to a failure rate of approximately 2%, which is considered acceptable. The primary cause of disconnection was attributed to non-uniform copper deposition within the via.

The LC injection procedure is as follows. CMP was performed on both quartz substrates to ensure flat surfaces. A 100-nm-thick polyimide alignment layer was applied to the metal surface using a spin coater, followed by a rubbing process to align the LC molecules. The resulting pretilt angle ranged from 0.6° to 1.2°, which does not significantly impact RF performance.

To maintain a uniform cell gap, 45 μm-diameter silica spacers were distributed across the surface. A sealing material was applied along the edges of both substrates, which were then bonded to form a cavity. The LC was subsequently injected under vacuum and sealed. To simplify the alignment process and facilitate LC injection, the two rectangular substrates were arranged in an L-shape, aligning at one corner.

After LC injection, a custom-designed flexible printed circuit (FPC) was attached to the RIS. Fig. 13 illustrates the schematic of the fabricated FPC. For stable voltage delivery, the RIS was designed with 1D biasing lines, incorporating 50 pads along one edge. The FPC consists of 50 corresponding lines: one end connects to the RIS, while the other is dimensioned to fit a commercial connector. This configuration ensures reliable electrical interfacing with the control circuitry and offers mechanical flexibility, which facilitates measurement without spatial constraints.

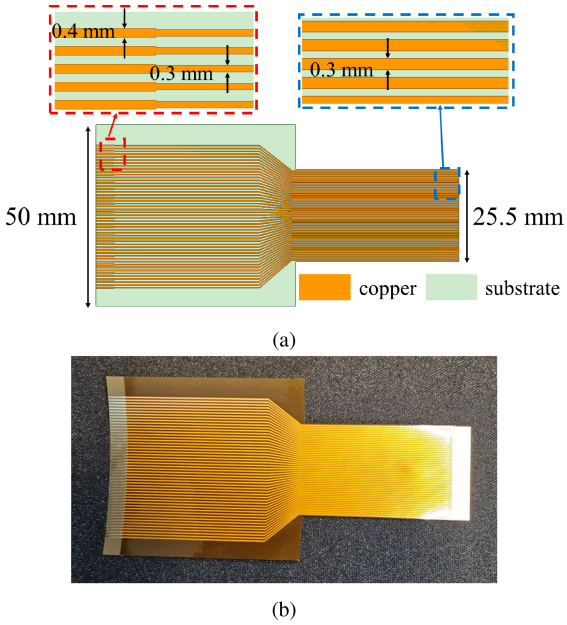

FIGURE 13. Custom-designed FPC used for interfacing the control circuit with the RIS. (a) Schematic diagram of the FPC layout; (b) fabricated FPC sample.

IV. EXPERIMENTAL VALIDATION OF THE PROPOSED RIS

Fig. 14 presents the fabricated RIS prototype and the measurement setup used for experimental validation. The overall dimensions of the fabricated RIS are 55 mm × 55 mm, while the active polarization conversion area measures 40 mm × 40 mm, corresponding to approximately 18.7λ × 18.7λ at 140 GHz.

A free-space measurement setup was employed to characterize the performance of the proposed RIS. The experimental apparatus included an Anritsu MS4647B vector network analyzer (VNA), VDI WR 6.5 waveguide extenders for both transmission and reception, a rotary platform, and a custom-designed control circuit. An acrylic jig was used to mount the transmitter (Tx) and align it with the RIS. The control circuit was managed using a laptop interface via PuTTY, while the rotary platform was controlled using its proprietary software. The control circuit and laptop communicated via a serial interface. A microcontroller unit (MCU), as shown in Fig. 14(c), was programmed to drive a digital-to-analog converter (DAC), converting digital control signals into the required DC voltages. A high-gain, narrow-beamwidth transmitarray antenna [31, pp. 137–145] was used to focus the transmitted beam and enhance measurement precision. For calibration, a gold-coated metal plate with the same dimensions as the RIS (shown in Fig. 11(a)) was used to perform standard free-space reference measurements. The normalized S_{21} was obtained by taking the ratio of the S_{21} measured with the RIS to that obtained with the reference metal plate.

The custom-designed FPC was connected to the control circuit via a commercial connector, allowing voltage control through the FPC. The RIS was configured to support 1D beam steering, with 50 voltage pads arranged along one edge of the surface, matching the 50 signal lines in the FPC.

The RIS beam steering control procedure is as follows. The required reflection phase for each column is calculated using

$$\phi_{\text{req}} = k_0 d(\sin(\phi_{\text{ref}}) - \sin(\phi_{\text{inc}})) \tag{5}$$

where ϕ_{req} is the required phase for each column, k_0 is the free-space wave number, $d = 0.8$ mm is the center-to-center distance between unit cells, ϕ_{inc} is the angle of incidence, and ϕ_{ref} is the reflection angle as defined in Fig. 14(a). Note that ϕ_{inc} is defined in the counterclockwise direction, while ϕ_{ref}

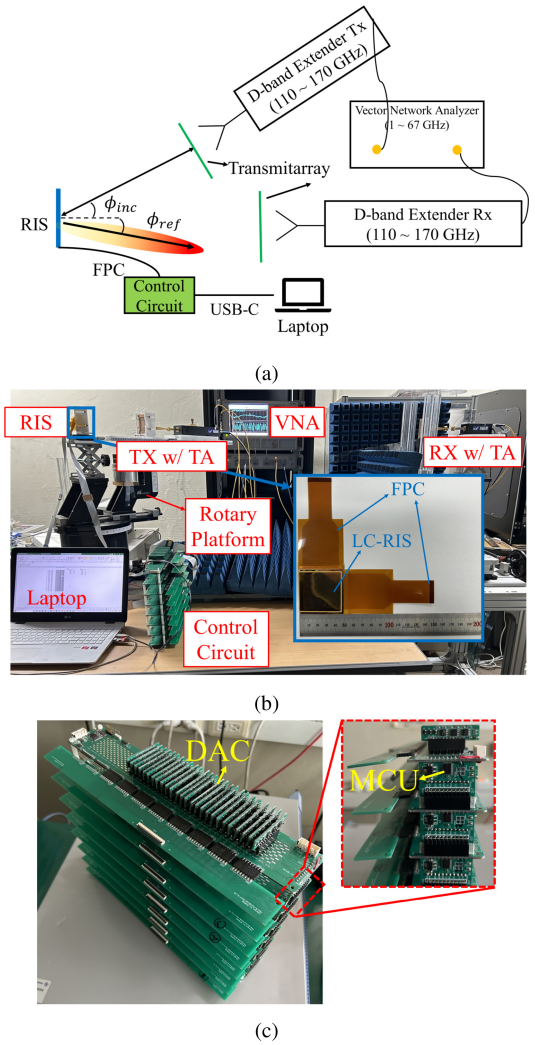

FIGURE 14. Free-space measurement setup for validating the proposed RIS using a transmitarray-based configuration. (a) Schematic diagram of the measurement setup; (b) photograph of the actual measurement system; (c) photograph of the control circuit.

is measured clockwise. The calculated phase profile is then compared with the achievable phase range of the LC unit cell to determine the appropriate bias voltages. These voltage values are converted to digital signals by the control laptop and transmitted to an FPGA via USB. The FPGA generates corresponding DC voltages, which are delivered to the RIS through the FPC. Finally, the S_{21} parameter was measured for reflection angles ϕ_{ref} ranging from 0° to 60° using the rotary platform, verifying the beam steering capability of the RIS. Angular sampling during measurements was 5°. For visualization, curves are rendered using shape-preserving cubic interpolation; all quantative metrics are computed from the raw 5°. The angular sampling uncertainty is reported as 2.5°.

A. UNIT CELL LEVEL PERFORMANCE

To evaluate the frequency response of the RIS unit cell, all bias lines were driven with the same voltage. As a result, phase distribution calculations were not required. A voltage of 0 V was applied to represent the unbiased state, and 23 V was applied to represent the fully biased state, both controlled via the FPGA.

For this measurement, the angles of incidence and reflection were set to be identical, i.e., $\phi_{\text{inc}} = \phi_{\text{ref}}$. Under these conditions, the entire RIS behaves as an infinite periodic array of identical unit cells in the same LC state, closely approximating the conditions used in Floquet-based full-wave electromagnetic simulations. It is worth noting that, due to the limitations of the measurement environment and the need to avoid feed blockage, normal incidence measurements (i.e., $\phi_{\text{inc}} = \phi_{\text{ref}} = 0°$ in Fig. 14(a)) could not be performed.

Fig. 15(a) and Fig. 15(b) present the measured frequency responses of the unit cell for the co-polarized and cross-polarized components. The results confirm that the proposed RIS effectively performs polarization conversion for both x-to-y and y-to-x incident waves. The polarization conversion efficiency peaks near the center frequency of 140 GHz; however, relatively high insertion losses are observed. The oblique-incidence responses, shown in Fig. 15(c) and (d), correspond to incident angles ranging from $\phi_{\text{inc}} = \phi_{\text{ref}} = 20°$ to 60°. For both x-to-y and y-to-x polarization conversions, a deviation within -1 dB is maintained over an angular range up to 45°, beyond which the polarization conversion performance rapidly degrades, with negligible response observed above 50°. It is important to note that polarization conversion resonances (e.g., at 140 GHz) inherently exhibit elevated reflection losses, which can cause the PCR to appear lower exactly where the polarization rotation is most effective. For this reason, we emphasize the direct co-polarized and cross-polarized reflection responses as more reliable indicators of polarization conversion behavior.

Fig. 16(a) and Fig. 16(b) compare the simulated and measured amplitude responses of the RIS. While both exhibit similar trends, noticeable discrepancies are present in the absolute values. Several factors contribute to this mismatch. First, the relative permittivity of the LC under full bias was assumed to be 3.5 in the simulation. However, measurements indicate that the actual permittivity is lower, and the loss tangent exceeds the assumed value of 0.023. These two material parameters significantly affect both amplitude and bandwidth. Second, the simulation model treats the LC as isotropic and homogeneous, whereas in practice, LC materials exhibit anisotropic and inhomogeneous behavior. This material anisotropy introduces deviations from the idealized model. To improve the agreement between simulation and measurement, we are currently integrating LC molecular orientation simulator with EM simulator. This approach enables spatial modeling of voltage-induced LC alignment and extraction of region-specific effective permittivities. Although RF losses and fabrication defects remain unmodeled, this method is expected to yield more accurate phase behavior in future simulations. Third, fabrication imperfections play a role. The sanding-based TQV formation process applies mechanical force, which can introduce microcracks or surface scratches in the quartz substrate.

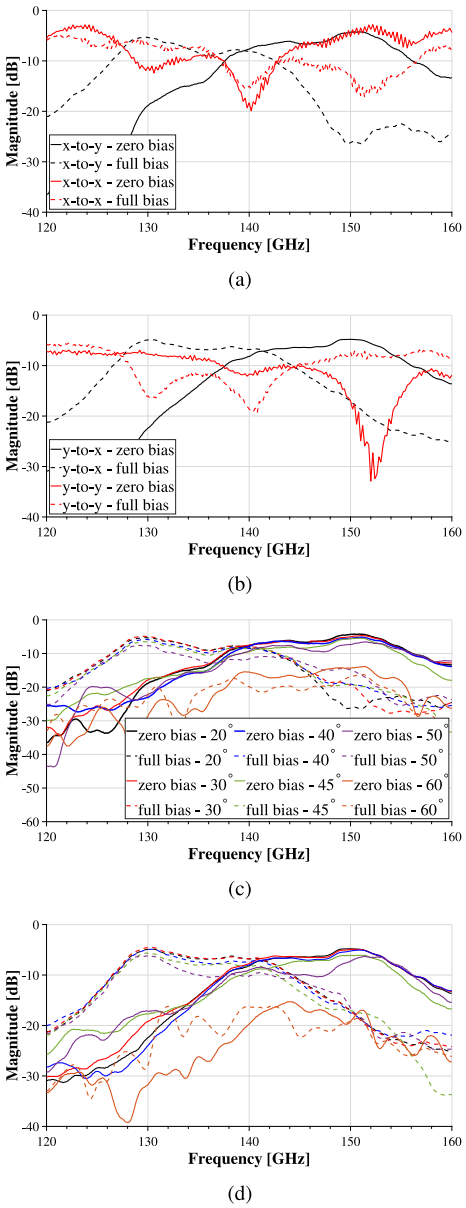

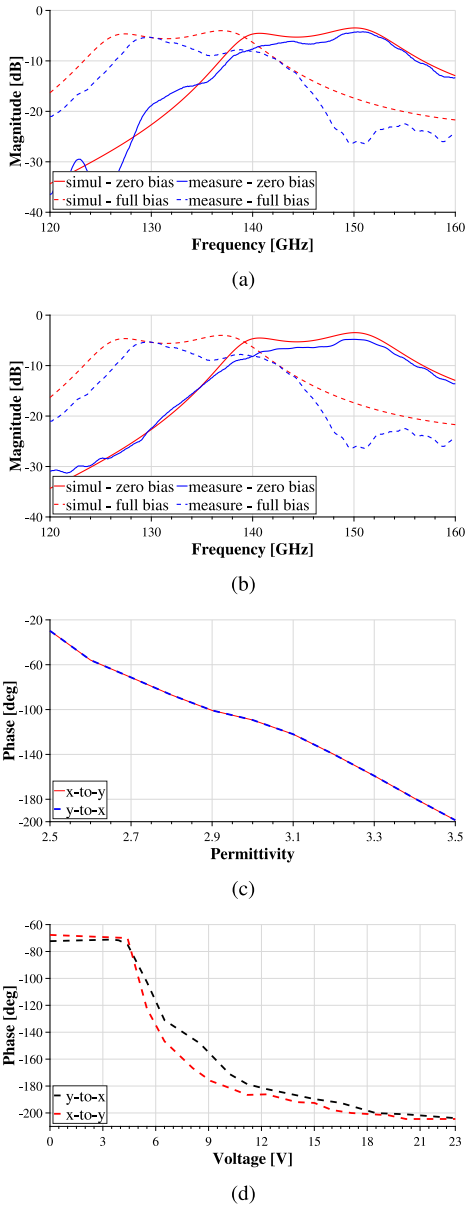

FIGURE 15. Measured frequency responses of the proposed unit cell under oblique incidence and various DC bias voltages. (a) Reflection magnitude for *x*-to-*y* and *x*-to-*x* polarizations at $\phi_{inc} = 20°$; (b) reflection magnitude for *y*-to-*x* and *y*-to-*y* polarizations at $\phi_{inc} = 20°$; (c) reflection magnitude for *x*-to-*y* polarization from $\phi_{inc} = 20°$ to 60°; (d) reflection magnitude for *y*-to-*x* polarization over the same angular range.

FIGURE 16. Comparison between simulated and measured responses under $\phi_{inc} = 20°$. (a) Amplitude responses for *x*-to-*y* polarizations; (b) amplitude responses for *y*-to-*x* polarizations; (c) simulated phase response as a function of LC permittivity; (d) measured phase response range for *x*-to-*y* and *y*-to-*x* polarizations.

In addition, not all TQVs were perfectly formed, leading to incomplete voltage delivery to some unit cells. These non-idealities contribute to measurement inconsistencies. Moreover, the rubbing direction, aligned along the *x*-axis in this study, may have introduced asymmetries that affect the *x*-to-*y* and *y*-to-*x* conversion balance.

Fig. 16(c) and Fig. 16(d) show the simulated and measured phase responses, respectively. The phase range was extracted following the method in [32], with bias voltages swept from 0 V to 23 V in 0.5 V increments. The measured phase range was 137°, approximately 31° lower than the simulation result. This reduction is primarily attributed to variations in the LC material properties and fabrication tolerances. It should be noted that establishing an explicit one-to-one relationship between voltage and effective permittivity is practically infeasible. For this reason, many prior studies on LC-based metasurfaces [23], [24], [33], [34] do not explicitly present the permittivity-voltage relationship. Instead, simulations typically illustrate the phase variation as a function of effective permittivity, while measurements report the phase shift directly as a function of applied voltage, often through a look-up table calibration approach [23].

One notable limitation of LC-based reconfigurable devices is their relatively slow response time compared to

TABLE 2. Comparison table of related research approaches.

	Frequency [GHz]	Tuning Mechanism	Phase-type	Array	Beam Steering	Polarization Conversion
[41]	4.25	Varactor	2-bit	16 × 8	✓	×
[42]	5.9	Varactor	1-bit	14 × 14	×	✓
[43]	27.5	PIN-diode	1-bit	20 × 20	✓	×
[14]	3.15	Varactor	3-bit	10 × 10	✓	×
[15]	5.5	Power amplifier	-	2 × 2	×	✓
[44]	7.4	Varactor	Continuous	15 × 15	✓	✓
[23]	28	Liquid crystal	Continuous	10 × 10	✓	×
[38]	130	Liquid crystal	×	×	×	✓
[39]	690	Liquid crystal	Continuous	40 × 40	✓	×
[40]	318.0-375.6	Liquid crystal	-	92 × 92	×	✓
This work	140	Liquid crystal	Continuous	50 × 50	✓	✓

semiconductor-based counterparts. While diodes typically operate with switching speeds in the nanosecond to microsecond range, LC materials exhibit response times on the order of milliseconds to seconds. For example, in the proposed structure with a 45 µm cell gap, the rise time is approximately 3–4 s, and the fall time is approximately 15–16 s. These values are consistent with those reported for other RF-grade LC materials [35]. Recent studies have focused on reducing the LC response time through several approaches, including the application of overdrive voltage techniques [36], the use of dual-frequency LCs [37], and the implementation of polymer network LCs [35].

B. RIS PERFORMANCE

Fig. 17 shows the measured S_{21} parameter for an incident angle of $\phi_{\text{inc}} = 20°$. The term "Bias Off" indicates that the control circuit is powered down, resulting in a zero-bias state for all LC elements. "Bias On" denotes that the control circuit is active, but without programmed voltage distribution for beam steering. In contrast, "RIS On" represents the condition where the RIS is actively biased to steer the reflected beam toward the desired angle ϕ_{ref}.

Measurements were conducted in 5° increments around the target reflection angle. Fig. 17(a) and (b) display the x-to-y polarization S_{21} when the RIS is configured to reflect toward $\phi_{\text{ref}} = 40°$. A notable gain of 19 dB is observed in the "RIS On" state at the intended direction compared to the "Bias On" and "Bias Off" states. The

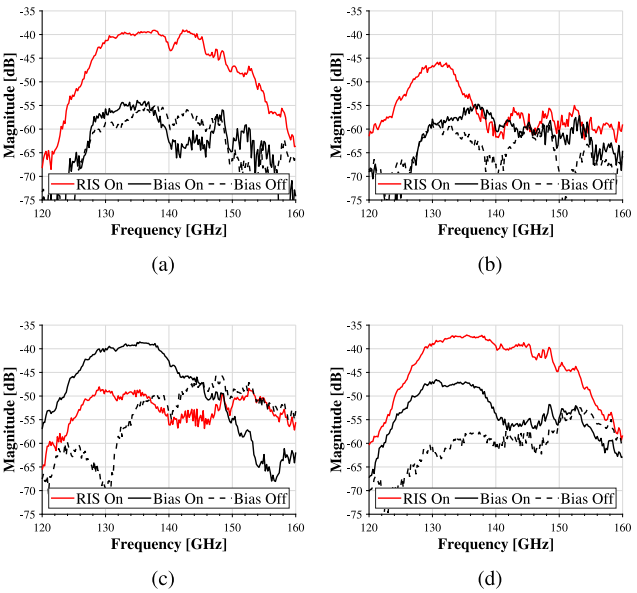

FIGURE 17. Measured S_{21} of the proposed RIS under an incident angle of $\phi_{\text{inc}} = 20°$. (a) x-to-y polarization with reflection angle $\phi_{\text{ref}} = 40°$; (b) x-to-y polarization with $\phi_{\text{ref}} = 45°$; (c) y-to-x polarization with $\phi_{\text{ref}} = 25°$; (d) y-to-x polarization with $\phi_{\text{ref}} = 30°$.

high magnitude observed for the "RIS On" state around 130 GHz in Fig. 17(b) can be explained by the beam squint phenomenon. The RIS was programmed with a phase gradient to steer the beam to 40° at the design frequency of 140 GHz. However, the steering angle of a phased array is

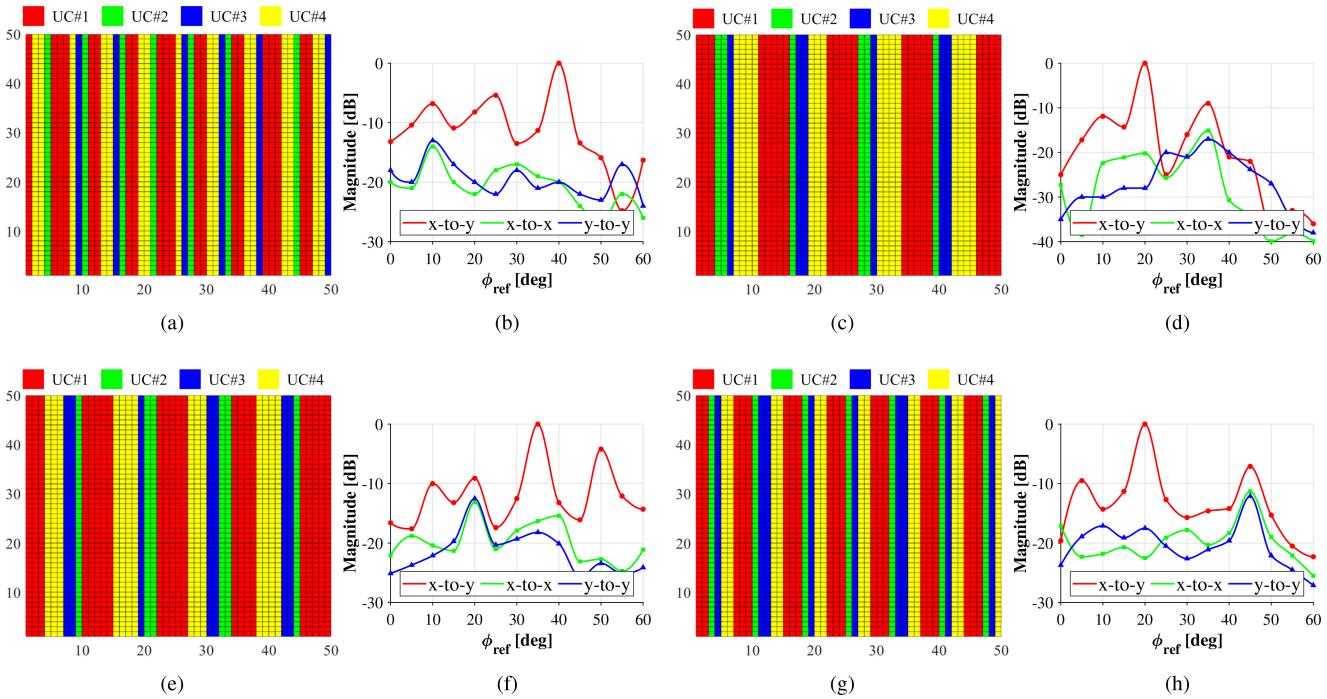

FIGURE 18. Normalized radiation patterns and corresponding phase distributions of the proposed RIS under various incident angles. Beam steering and polarization conversion are verified by analyzing *x*-to-*y*, *y*-to-*x*, *x*-to-*x*, and *y*-to-*y* responses. (a) Phase distribution for *x*-to-*y* conversion at $\phi_{inc} = 10°$ and $\phi_{ref} = 40°$; (b) corresponding radiation pattern. (c) Phase distribution for *x*-to-*y* at $\phi_{inc} = 35°$ and $\phi_{ref} = 20°$; (d) corresponding radiation pattern. (e) Phase distribution for *y*-to-*x* at $\phi_{inc} = 45°$ and $\phi_{ref} = 20°$; (f) corresponding radiation pattern. (g) Phase distribution for *y*-to-*x* at $\phi_{inc} = 20°$ and $\phi_{ref} = 35°$; (h) corresponding radiation pattern.

frequency-dependent. Our array factor analysis confirms that this fixed phase gradient steers the beam to approximately 45° at 130 GHz. Since the measurement in Fig. 17(b) was performed with the receiver at 45°, the high S21 magnitude is a direct result of the main beam at 130 GHz being aligned with the receiver.

Fig. 17(c) and (d) present the *y*-to-*x* polarization results when the RIS is steered toward $\phi_{ref} = 30°$. At $\phi_{ref} = 25°$, the "RIS On" response is lower than in the other two states, whereas at $\phi_{ref} = 30°$, a 20 dB improvement is observed in the "RIS On" state at 140 GHz.

Fig. 18 shows the normalized radiation patterns for multiple incident angles and polarization configurations. The beam steering and polarization conversion capabilities were verified by comparing *x*-to-*y*, *y*-to-*x*, *x*-to-*x*, and *y*-to-*y* responses. Voltage control was based on the phase profile calculated using (5), with the corresponding voltages applied through the control circuit.

Fig. 18(a), (c), (e), and (g) present the applied phase distributions, using four LC states: 0 V: –70° (UC#1), 6 V: –115° (UC#2), 8 V:–155° (UC#3), and 23 V: –203° (UC#4). The *x*-to-*y* patterns for $\phi_{inc} = 10°$ and 35° (Fig. 18(b) and (d)) exhibit maximum gain at $\phi_{ref} = 40°$ and 20°, respectively. Due to the presence of the ground plane, specular reflections are observed at the same angles as the incidence. The side-lobe levels were measured at −5.4 dB and −9 dB, respectively, which are acceptable given the phase range limitations. Similarly, Fig. 18(f) and (h) show the *y*-to-*x* radiation patterns for $\phi_{inc} = 45°$ and 20°, with side-lobe levels of −4.2 dB and −7.1 dB, respectively. These results confirm that the proposed RIS achieves simultaneous beam steering and polarization conversion as designed.

Table 2 summarizes recent related works on RIS. Compared to prior studies, the proposed structure is among the first to demonstrate an LC-based RIS operating in the sub-THz regime. The proposed RIS was specifically optimized to operate at 140 GHz. Although simulations indicate a –6 dB polarization conversion bandwidth from 138.1 GHz to 141.69 GHz, measured reflection loss was substantially higher across the band, limiting the effective operational frequency to approximately 140 GHz. In contrast to diode-based designs-which are unsuitable for sub-THz applications due to their self-resonant frequencies-LC technology provides continuous phase tunability via a simple biasing network.

A key contribution of this work is the integration of TQVs formed via the sanding technique to maintain polarization conversion characteristics, which has not been reported in other LC-based RIS designs. For instance, [38] reports an LC-based polarization converter for sub-THz, capable of switching between linear and circular polarization based on the incidence angle. However, beam steering was not demonstrated, and no fabricated samples were presented. Reference [39] reports an LC-based programmable metasurface at THz band. It can steer the beam but cannot convert polarization. Reference [40] reports an LC-based polarization converter for THz band, capable of switching between linear and circular polarization.

V. CONCLUSION

This paper presented an LC-based RIS capable of dual-polarization conversion in the sub-THz band, incorporating a TQV structure. The proposed design integrates a ring-shaped patch and a diagonal stub to achieve simultaneous polarization conversion, while also maintaining a dynamic and tunable phase range suitable for beam steering applications. To preserve polarization conversion performance, TQVs were introduced through the quartz substrate, enabling bias line routing without compromising electromagnetic behavior. Both full-wave simulations and experimental measurements confirmed that the inclusion of TQVs had minimal impact on the unit cell's frequency and polarization characteristics. The polarization conversion efficiency and reflected signal strength were experimentally validated under various beam steering conditions. Additionally, the radiation patterns of the RIS were evaluated across multiple incidence angles, demonstrating reliable beam directionality and cross-polarization conversion.

The outcomes of this work contribute to the development of high-frequency RIS technology and provide a viable design pathway for future 6G wireless communication systems operating in the sub-THz regime.

REFERENCES

[1] Samsung, *White Paper: 6G Spectrum Expanding the Frontier*, (2020). [Online]. Available: https://research.samsung.com/next-generation-communications

[2] W. Jiang, B. Han, M. A. Habibi, and H. D. Schotten, "The road towards 6G: A comprehensive survey," *IEEE Open J. Commun. Soc.*, vol. 2, pp. 334–366, 2021.

[3] (NTT Docomo, Chiyoda, Japan). *White Paper: 5G Evolution and 6G*. (2022). [Online]. Available: https://www.docomo.ne.jp/english/corporate/technology/whitepaper6g/

[4] A. Altaf, M. Elahi, S. M. Abbas, J. Yousaf, and E. Almajali, "A D-band waveguide-SIW transition for 6G applications," *J. Electromagn. Eng. Sci.*, vol. 22, no. 4, pp. 419–426, 2022.

[5] K. Rikkinen, P. Kyosti, M. E. Leinonen, M. Berg, and A. Parssinen, "THz radio communication: Link budget analysis toward 6G," *IEEE Commun. Mag.*, vol. 58, no. 11, pp. 22–27, Nov. 2020.

[6] M. Matthaiou, O. Yurduseven, H. Q. Ngo, D. Morales-Jimenez, S. L. Cotton, and V. F. Fusco, "The road to 6G: Ten physical layer challenges for communications engineers," *IEEE Commun. Mag.*, vol. 59, no. 1, pp. 64–69, Jan. 2021.

[7] S. Inoué, "Video image processing greatly enhances contrast, quality, and speed in polarization-based microscopy," *J. Cell Biol.*, vol. 89, no. 2, pp. 346–356, 1981.

[8] M. Zhang, W. Zhang, A. Q. Liu, F. Li, and C. Lan, "Tunable polarization conversion and rotation based on a reconfigurable metasurface," *Sci. Rep.*, vol. 7, no. 1, pp. 1–7, 2017.

[9] Z. Zhang, C. Zhong, F. Fan, G. Liu, and S. Chang, "Terahertz polarization and chirality sensing for amino acid solution based on chiral metasurface sensor," *Sens. Actuat. B, Chem.*, vol. 330, Mar. 2021, Art. no. 129315.

[10] C. Dietlein, A. Luukanen, Z. Popovi, and E. Grossman, "A W-band polarization converter and isolator," *IEEE Trans. Antennas Propagat.*, vol. 55, no. 6, pp. 1804–1809, Jun. 2007.

[11] A. Ren et al., "State-of-the-art in terahertz sensing for food and water security—A comprehensive review," *Trends Food Sci. Technol.*, vol. 85, pp. 241–251, Mar. 2019.

[12] T. J. Cui, M. Q. Qi, X. Wan, J. Zhao, and Q. Cheng, "Coding metamaterials, digital metamaterials and programmable metamaterials," *Light, Sci. Appl.*, vol. 3, no. 10, pp. e218–e218, 2014.

[13] S. Y. Miao and F. H. Lin, "Light-controlled large-scale wirelessly reconfigurable microstrip reflectarrays," *IEEE Trans. Antennas Propag.*, vol. 71, no. 2, pp. 1613–1622, Feb. 2023.

[14] J. C. Liang et al., "An angle-insensitive 3-bit reconfigurable intelligent surface," *IEEE Trans. Antennas Propag.*, vol. 70, no. 10, pp. 8798–8808, Oct. 2022.

[15] L. Wu et al., "A wideband amplifying reconfigurable intelligent surface," *IEEE Trans. Antennas Propag.*, vol. 70, no. 11, pp. 10623–10631, Nov. 2022.

[16] J.-B. Gros, V. Popov, M. A. Odit, V. Lenets, and G. Lerosey, "A reconfigurable intelligent surface at mmWave based on a binary phase tunable metasurface," *IEEE Open J. Commun. Soc.*, vol. 2, pp. 1055–1064, 2021.

[17] G. C. Trichopoulos et al., "Design and evaluation of reconfigurable intelligent surfaces in real-world environment," *IEEE Open J. Commun. Soc.*, vol. 3, pp. 462–474, 2022.

[18] L. Dai et al., "Reconfigurable intelligent surface-based wireless communications: Antenna design, prototyping, and experimental results," *IEEE Access*, vol. 8, pp. 45913–45923, 2020.

[19] F. Yang, P. Pitchappa, and N. Wang, "Terahertz reconfigurable intelligent surfaces (RISs) for 6G communication links," *Micromachines*, vol. 13, no. 2, p. 285, 2022.

[20] S. Bang, H. Kim, and J. Oh, "Enhancing 2-D beam scanning capability through extended transmission paths in a liquid crystal-based transmitarray antenna for mmWave communications," *J. Electromagn. Eng. Sci.*, vol. 25, no. 1, pp. 85–91, 2025.

[21] D. Kim et al., "Characterization of nematic liquid crystal dielectric properties using complementary FSSs featuring electrically small cell gaps across a wide sub-THz range," *IEEE Trans. Antennas Propag.*, vol. 72, no. 2, pp. 2019–2024, Feb. 2024.

[22] X. Liu, Y. Ge, X. Chen, and L. Chen, "Design of folded reflectarray antennas using Pancharatnam-Berry phase reflectors," *IEEE Access*, vol. 6, pp. 28818–28824, 2018.

[23] H. Kim, S. Oh, S. Bang, H. Yang, B. Kim, and J. Oh, "Independently Polarization manipulable liquid- crystal -based reflective Metasurface for 5G Reflectarray and reconfigurable intelligent surface," *IEEE Trans. Antennas Propag.*, vol. 71, no. 8, pp. 6606–6616, Aug. 2023.

[24] X. Li, H. Sato, Y. Shibata, T. Ishinabe, H. Fujikake, and Q. Chen, "Development of beam steerable reflectarray with liquid crystal for both E-plane and H-plane," *IEEE Access*, vol. 10, pp. 26177–26185, 2022.

[25] M. Ali, K.-Q. Huang, M. Swaminathan, P. M. Raj, and R. R. Tummala, "Laminated glass-based, compact inline stepped-impedance resonator bandpass filters for 5G new radio modules," *IEEE Trans. Compon., Packag. Manuf. Technol.*, vol. 11, no. 4, pp. 708–711, Apr. 2021.

[26] W. Zhang, J. Gu, L. Li, and X. Li, "Through-glass-via based microstrip band-pass filters fabricated with wafer-level low-melting-point alloy micro-casting," *IEEE Electron Device Lett.*, vol. 41, no. 7, pp. 1106–1109, Jul. 2020.

[27] X. Liu, Z. Zhu, Y. Liu, Q. Lu, X. Yin, and Y. Yang, "Compact bandpass filter and diplexer with wide-stopband suppression based on balanced substrate-integrated waveguide," *IEEE Trans. Microw. Theory Tech.*, vol. 69, no. 1, pp. 54–64, Jan. 2021.

[28] N. Liu, X. Liu, Y. Liu, Y. Yang, and Z. Zhu, "Compact interdigital bandpass filter, diplexer, and triplexer based on through quartz vias (TQVs)," *IEEE Trans. Compon., Packag. Manuf. Technol.*, vol. 12, no. 6, pp. 988–997, Jun. 2022.

[29] Y. Su, D. Yu, W. Ruan, and N. Jia, "Development of compact millimeter-wave antenna by stacking of five glass wafers with through glass vias," *IEEE Electron Device Lett.*, vol. 43, no. 6, pp. 934–937, Jun. 2022.

[30] M. J. Laakso et al., "Through-glass vias for glass interposers and MEMS packaging applications fabricated using magnetic assembly of microscale metal wires," *IEEE Access*, vol. 6, pp. 44306–44317, 2018.

[31] S. Oh, "Reconfigurable intelligent surface assisted beamforming in hyper-connected metasurface antenna-RFIC packaging systems for 6G networks," Ph.D. dissertation, Dept. Electr. Comput. Eng., College Eng., Seoul Nat. Univ., Seoul, South Korea, 2023.

[32] H. Kim, J. Kim, and J. Oh, "Communication a novel systematic design of high-aperture-efficiency 2D beam-scanning liquid-crystal embedded reflectarray antenna for 6G FR3 and radar applications," *IEEE Trans. Antennas Propag.*, vol. 70, no. 11, pp. 11194–11198, Nov. 2022.

[33] W. Hu et al., "Design and measurement of reconfigurable millimeter wave reflectarray cells with nematic liquid crystal," *IEEE Trans. Antennas Propag.*, vol. 56, no. 10, pp. 3112–3117, Oct. 2008.

[34] G. Perez-Palomino et al., "Design and experimental validation of liquid crystal-based reconfigurable reflectarray elements with improved bandwidth in F-band," *IEEE Trans. Antennas Propag.*, vol. 61, no. 4, pp. 1704–1713, Apr. 2013.
[35] R. Guirado, G. Perez-Palomino, M. Caño-García, M. A. Geday, and E. Carrasco, "Mm-wave metasurface unit cells achieving millisecond response through polymer network liquid crystals," *IEEE Access*, vol. 10, pp. 127928–127938, 2022.
[36] R. Guirado, G. Perez-Palomino, M. Ferreras, E. Carrasco, and M. Caño-García, "Dynamic modeling of liquid crystal-based metasurfaces and its application to reducing reconfigurability times," *IEEE Trans. Antennas Propag.*, vol. 70, no. 12, pp. 11847–11857, Dec. 2022.
[37] R. Guirado, P. De la Rosa, G. Perez-Palomino, M. Caño-García, E. Carrasco, and X. Quintana, "Characterization and application of dual frequency liquid crystal mixtures in mm-wave Reflectarray cells to improve their temporal response," *IEEE Trans. Antennas Propag.*, vol. 71, no. 8, pp. 6535–6545, Aug. 2023.
[38] E. Doumanis et al., "Electronically reconfigurable liquid crystal based mm-wave polarization converter," *IEEE Trans. Antennas Propag.*, vol. 62, no. 4, pp. 2302–2307, Apr. 2014.
[39] T. Wang et al., "A liquid-crystal-based programmable metasurface for full-space terahertz beam steering," *J. Appl. Phys.*, vol. 138, no. 3, 2025, Art. no. 33105.
[40] G. Deng, Y. Zhu, Q. Zhang, J. Yang, Y. Li, and Z. Yin, "Reconfigurable dual-functional reflective Polarization converter based on liquid crystal terahertz metasurfaces," *IEEE Trans. Antennas Propag.*, vol. 73, no. 6, pp. 4164–4169, Jun. 2025.
[41] C. Zhang et al., "Convolution operations on time-domain digital coding metasurface for beam manipulations of harmonics," *Nanophotonics*, vol. 9, no. 9, pp. 2771–2781, 2020.
[42] J. Y. Dai et al., "Arbitrary manipulations of dual harmonics and their wave behaviors based on space-time-coding digital metasurface," *Appl. Phys. Rev.*, vol. 7, no. 4, 2020, Arty. no. 41408.
[43] X. Gao, W. L. Yang, H. F. Ma, Q. Cheng, X. H. Yu, and T. J. Cui, "A reconfigurable broadband polarization converter based on an active metasurface," *IEEE Trans. Antennas Propag.*, vol. 66, no. 11, pp. 6086–6095, Nov. 2018.
[44] M. Wang, D. Liao, J. Y. Dai, and C. H. Chan, "Dual-polarized reconfigurable metasurface for multifunctional control of electromagnetic waves," *IEEE Trans. Antennas Propag.*, vol. 70, no. 6, pp. 4539–4548, Jun. 2022.

BYEONGJU MOON (Student Member, IEEE) received the B.S. degree from Sungkyunkwan University, South Korea, in 2021. He is currently pursuing an integrated M.S. and Ph.D. degrees with the Department of Electrical and Computer Engineering, Seoul National University, South Korea. His current research interests include metasurfaces, reconfigurable intelligent surfaces for B5G/6G communication, millimeter-wave radar systems, and integrated sensing and communication antenna.

SEUNGWOO BANG (Graduate Student Member, IEEE) received the B.S. degree from the Seoul National University of Science and Technology, South Korea, in 2022. He is currently pursuing an integrated M.S. and Ph.D. degrees with the Department of Electrical and Computer Engineering, Seoul National University, South Korea. His current research interests include metasurfaces and antenna design.

SEONGWOOG OH (Member, IEEE) received the B.S. degree in electrical engineering and computer science from the Gwangju Institute of Science and Technology College, Gwangju, South Korea, in 2016, and the M.S. and Ph.D. degrees in electrical engineering from Seoul National University, Seoul, South Korea, in 2018 and 2023, respectively.

From 2023 to 2024, he was with the TICS Research Group, Department of Electrical and Computer Engineering, University of California at San Diego as a Postdoctoral Researcher. From 2024 to 2025, he was a Faculty Member with the Department of Electronics Convergence Engineering, Kwangwoon University, South Korea. He is currently an Assistant Professor with the School of Electrical and Computer Engineering, University of Seoul, South Korea. His research interests include the design of RF/millimerter-wave integrated circuits, antenna-on-package systems for 5G/6G communication, nuclear fusion antennas, and microwave bio-applications. He was a recipient of the 2019 IEEE MTT Seoul Chapter Best Paper Award, the 2022 IEEE AP-S Student Paper Competition Honorable Mention, and the 2022 IEEE Antennas and Propagation Society Fellowship.

JUNGSUEK OH (Senior Member, IEEE) received the B.S. and M.S. degrees from Seoul National University, South Korea, in 2002 and 2007, respectively, and the Ph.D. degree from the University of Michigan at Ann Arbor in 2012. From 2007 to 2008, he worked with Korea Telecom as a Hardware Research Engineer, and was involved with the development of flexible RF devices. In 2012, he was a Postdoctoral Research Fellow with the Radiation Laboratory, University of Michigan at Ann Arbor. From 2013 to 2014, he was a Staff RF Engineer with Samsung Research America, Dallas, where he worked as a Project Leader for a 5G/millimeter-wave antenna system. From 2015 to 2018, he was a Faculty Member with the Department of Electronic Engineering, Inha University, South Korea. He is currently an Assistant Professor with the School of Electrical and Computer Engineering, Seoul National University, South Korea. He has published more than 40 technical journal and conference papers. His research areas include mmWave beam focusing/shaping techniques, antenna miniaturization for integrated systems, and radio propagation modeling for indoor scenarios. He was the recipient of the 2011 Rackham Predoctoral Fellowship Award at the University of Michigan at Ann Arbor. He has served as a Technical Reviewer for (among other journals) the IEEE TRANSACTIONS ON ANTENNAS AND PROPAGATION and IEEE ANTENNAS AND WIRELESS PROPAGATION LETTERS. He has served as a TPC Member and a Session Chair for the IEEE AP-S/USNC-URSI and ISAP.